CT image segmentation of bone for medical additive manufacturing using a convolutional neural network

Jordi Minnema[a,*], Maureen van Eijnatten[a,c], Wouter Kouw[b], Faruk Diblen[b], Adriënne Mendrik[b], Jan Wolff[a,d]

[a] Amsterdam UMC and Academic Centre for Dentistry Amsterdam (ACTA), Vrije Universiteit Amsterdam, Department of Oral and Maxillofacial Surgery/Pathology, 3D Innovation Lab, Amsterdam Movement Sciences, de Boelelaan 1117, Amsterdam, the Netherlands
[b] Netherlands eScience Center, Science Park 140, Amsterdam, the Netherlands
[c] Centrum Wiskunde & Informatica (CWI), Science Park 123, Amsterdam, the Netherlands
[d] Department of Oral and Maxillofacial Surgery, Division for Regenerative Orofacial Medicine, University Hospital Hamburg-Eppendorf, Hamburg, Germany

ARTICLE INFO

ABSTRACT

Background: The most tedious and time-consuming task in medical additive manufacturing (AM) is image segmentation. The aim of the present study was to develop and train a convolutional neural network (CNN) for bone segmentation in computed tomography (CT) scans.
Method: The CNN was trained with CT scans acquired using six different scanners. Standard tessellation language (STL) models of 20 patients who had previously undergone craniotomy and cranioplasty using additively manufactured skull implants served as "gold standard" models during CNN training. The CNN segmented all patient CT scans using a leave-2-out scheme. All segmented CT scans were converted into STL models and geometrically compared with the gold standard STL models.
Results: The CT scans segmented using the CNN demonstrated a large overlap with the gold standard segmentation and resulted in a mean Dice similarity coefficient of 0.92 ± 0.04. The CNN-based STL models demonstrated mean surface deviations ranging between $-0.19\,mm \pm 0.86\,mm$ and $1.22\,mm \pm 1.75\,mm$, when compared to the gold standard STL models. No major differences were observed between the mean deviations of the CNN-based STL models acquired using six different CT scanners.
Conclusions: The fully-automated CNN was able to accurately segment the skull. CNNs thus offer the opportunity of removing the current prohibitive barriers of time and effort during CT image segmentation, making patient-specific AM constructs more accesible.

1. Introduction

Additive manufacturing (AM), also referred to as three-dimensional (3D) printing, is a technique in which successive layers of material are deposited on a build bed, allowing the fabrication of objects with complex geometries [1,2]. In medicine, additive manufactured tangible models are being increasingly used to evaluate complex anatomies [3,4]. Moreover, AM can be used to fabricate patient-specific constructs such as drill guides, saw guides, and medical implants. Such constructs can markedly reduce operating times and enhance the accuracy of surgical procedures [4]. AM constructs have proven to be particularly valuable in the field of oral and maxillofacial surgery due to the plethora of complex bony geometries found in the skull area.

The current medical AM process comprises four different steps: 1) image acquisition; 2) image processing; 3) computer-aided design; and 4) additive manufacturing (Fig. 1). Image acquisition is commonly performed using computed tomography (CT) since it offers the best hard tissue contrast [5]. During step 2 of the medical AM process, the acquired CT scan needs to be converted into a 3D surface model in the standard tessellation language (STL) file format. This STL model can be used to design patient-specific constructs (step 3) that can subsequently be fabricated using a 3D printer (step 4).

The most important step in the CT-to-STL conversion process is image segmentation: the partitioning of images into regions of interest that correspond to a specific anatomical structure (e.g., "bone"). To date, the most commonly used image segmentation method in medical AM is global thresholding [6]. However, global thresholding does not take CT artifacts and noise into account, nor the intensity variations
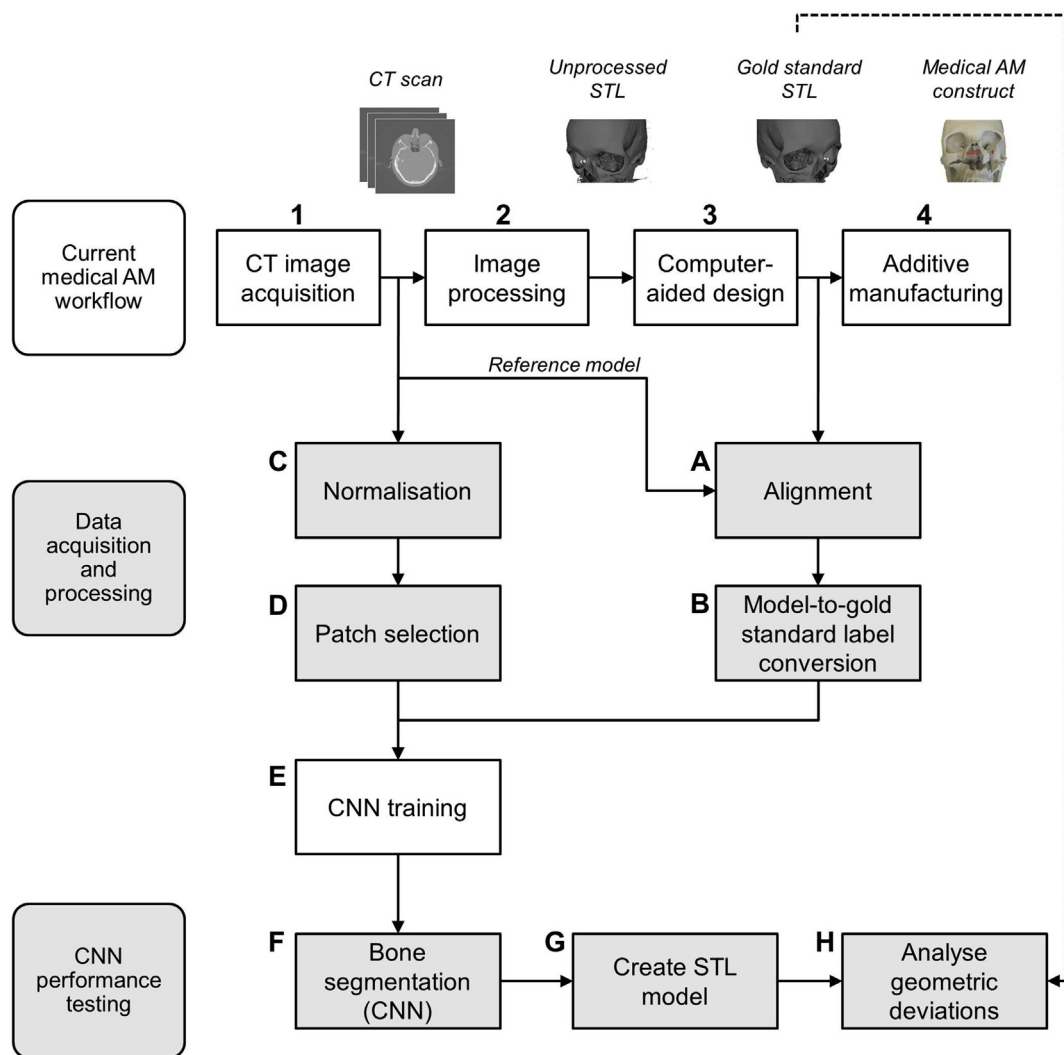
Fig. 1. Schematic overview of the study. The current medical additive manufacturing (AM) workflow is presented in the top of the figure. CT scans and STL models acquired in this process were used to train a convolutional neural network (CNN).

between different CT scanners that often results in inconsistent segmentation results [7]. Therefore, extensive manual post-processing and anatomical modeling is often indispensable. Moreover, due to subjectivity, fatigue, and variance amongst medical engineers, the quality of threshold-based image segmentations can differ markedly.

Many alternative (semi-)automatic image segmentation methods such as edge detection, region growing, statistical shape models, atlas-based methods, morphological snakes, active contouring, and random forests, have been developed over the last decades [6,8]. These automated methods are suitable to some extent for segmenting images with intensity inhomogeneities but often fail when applied to images acquired using different CT scanners and imaging protocols with varying noise levels. The inherent limitations have subsequently dampened the enthusiasm amongst physicians with an interest in adapting AM in clinical settings. Therefore, new methods to automate image segmentation are sought.

Over the past few years, there have been unparalleled advances in the field of artificial intelligence, especially after the ground-breaking performance of the convolutional neural network (CNN) developed by Alex Krizhevsky for the ImageNet challenge in 2012 [9]. A CNN is structured in layers. Each layer comprises multiple computational building blocks called neurons that share weighted connections with neurons in subsequent layers. During training, these layers extract features from training images, after which the CNN can recognize these

features in new, unseen images to perform a certain task, such as segmentation.

The aim of the present study was to develop and train a CNN for skull segmentation in CT scans. The CNN was trained using a unique patient dataset that represented variations that are commonly found in clinical CT scans. This will hopefully help overcome the aforementioned segmentation issues in medical AM and reduce the time-consuming and costly role of manual processing.

1.1. Related work

Traditionally, (semi-)automatic rule-based methods, such as edge detection [10], region based-methods [11,12], and level sets [13,14], have been used for medical image segmentation. The main strength of such rule-based approaches is their computational efficiency in terms of time and memory. Rule-based methods require the construction of generic priors to ensure correct segmentation. However, defining such generic priors is often a manual task, which can be cumbersome when segmenting images with high noise-levels or artifacts. Therefore, data-driven approaches were developed. Data-driven approaches do not depend on a fixed set of manually chosen rules but aim to extract relevant information from large numbers of medical images. Examples of data-driven approaches that have been frequently used for medical image segmentation are random forests [15,16], statistical shape

models [17–19], and atlas-based approaches [20,21]. Although many of these approaches offer more accurate segmentation results than rule-based methods, data-driven methods still lack the generalizability to segment medical images of varying shapes, sizes and properties [8]. Moreover, data-driven methods often fail when applied to images acquired using different CT scanners and imaging protocols.

One way to overcome these limitations is to use deep learning algorithms. Recent advances in Graphical Processing Units (GPU) computing have enabled the development of efficient and intelligent deep learning approaches [22]. More specifically, convolutional neural networks (CNNs) have opened up a wealth of promising opportunities across a number of image-based disciplines. For example, Prasoon et al. (2013) successfully employed a CNN for the segmentation of knee cartilage in magnetic resonance (MR) images [23]. They demonstrated the potential of CNNs and outperformed the then state-of-the-art k-Nearest Neighbor classification method. This has motivated many researchers to use CNNs for various medical segmentation tasks, such as the segmentation of brain tissue [24–26], prostate [27], bone [28,29], and tumors [30–33] in MR images. Furthermore, multiple studies have been conducted on the segmentation of kidneys [34] and the pancreas [35–37] in CT scans. A few studies have investigated the use of CNNs for bone segmentation in CT scans. For example, Vania et al. (2017) employed a CNN for the segmentation of the spine [38]. Moreover, Išgum et al. (2018) proposed an iterative CNN for the segmentation of vertebrae that outperformed alternative segmentation methods [39].

2. Novelties

The novelty of the present study is that it demonstrates the feasibility of training a CNN on a patient dataset for which a unique, high-quality gold standard was available, namely, STL models created by experienced medical engineers. To the best of our knowledge, no studies have been performed in which such "engineered" STL models were used as gold standard. Moreover, CT scans were acquired using different CT scanners and acquisition protocols in order to represent the variability that is commonly found amongst clinical CT datasets.

3. Materials and methods

This study followed the principles of the Helsinki Declaration and was performed in accordance with the guidelines of the Medical Ethics Committee of the VU University Medical Center Amsterdam. The Dutch Medical Research Involving Human Subjects Act (WMO) did not apply to this study (Ref: 2017.145).

3.1. Data acquisition

The CNN was trained using CT scans and STL models of 20 patients who had previously undergone craniotomy and cranioplasty using additively manufactured skull implants. The 20 CT scans were acquired using different CT scanners and imaging protocols in order to represent the variability that is commonly found amongst clinical CT datasets (Table 1). The bony structures in all 20 patient CT scans were initially segmented using global thresholding combined with manual corrections, i.e., removal of noise, artifacts and unrelated structures, such as the head rest in the CT scan, using the available segmentation editing tools in Mimics software (Mimics v20.0, Materialise, Leuven, Belgium). Medical engineers subsequently converted the segmented CT scans into STL models and imported these STL models into medical computer-aided design 3-matic software (3-matic v11.0, Materialise, Leuven, Belgium) for post-processing. The post-processing procedure included the removal of unconnected triangles (noise), the closing of unnatural gaps, and the smoothening of defect edges in the skull (Fig. 1, step 3). Hence, these post-processed STL models contained information that had been directly defined by medical engineers, and therefore served as the gold standard in our study.

3.2. Data processing: generating gold standard labels

All 20 gold standard STL models were subsequently used to create gold standard labels, namely "bone" or "background". To this end, all STL models had to be aligned with their corresponding CT scans (Fig. 1, step 'A'). Each STL model was aligned on a reference model with the same orientation as the CT scan using a local best-fit algorithm in GOM Inspect® software (GOM Inspect 2017, GOM GmbH, Braunschweig, Germany). The aligned STL models were subsequently converted into gold standard labels using the mesh-to-label conversion [40] module in 3D Slicer software (v. 4.6.2) (Fig. 1, step 'B') [41,42].

3.3. Data processing: generating patches

All 20 CT scans were normalized by rescaling the voxel values between 0 and 1 (Fig. 1, step 'C'). Normalization was performed as follows:

$$xnorm = \frac{x - CT\min}{CT\max - CT\min}, \tag{1}$$

where x_{norm} is the normalized voxel value between 0 and 1, x is the voxel intensity (in Hounsfield Units), CT_{min} is the minimum voxel intensity (in Hounsfield units), and CT_{max} is the maximal voxel intensity (in Hounsfield units) in the CT scan.

The normalized CT scans were used to select voxels from a confined rectangular region of interest within each 2D axial CT slice that contained bone (Fig. 2A). These voxels were subsequently used to create 33x33 patches centered on each voxel (Fig. 2B). Thus the created patches contained the intensity values of the surrounding voxels. The patches were then used to train the CNN to classify the center voxel of each patch as either "bone" or "background" (Fig. 1, step 'E').

Selecting patches from CT scans is a highly data imbalanced problem since bone voxels comprise only a small part of the total number of voxels. Training the CNN using the true distribution of bone voxels would cause the CNN to be biased towards classifying background voxels. Therefore, a balanced dataset was used to train the CNN, as proposed by Havaei et al. [30]. This means that an equal number of "bone" patches and "background" patches were randomly selected from the 20 CT scans, which resulted in 1 000 000 patches for each class, hence 2 000 000 patches in total.
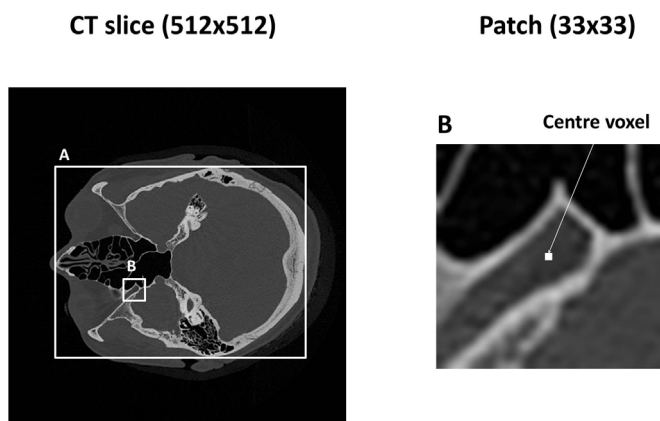
3.4. CNN architecture

The CNN architecture used in this study (Fig. 3) was initially developed by N. Aldenborgh for tumor segmentation in MR images [43]. The authors of the present study substantially adapted the aforementioned CNN for bone segmentation in CT images. One of the major differences between the current CNN and the CNN developed by Aldenborgh was the number of labels and input channels used to feed the CNN. Aldenborgh used 5 labels to segment different anatomical structures in MR images of the brain, whereas the modified algorithm implemented in this study used 2 labels to segment CT images into "bone" and "background" (air and soft tissues). In addition, Aldenborgh used 4 input channels to train their CNN on 4 different MRI sequences, whereas we used one input channel. Full details of our CNN architecture and settings can be publicly accessed online [44].

The CNN architecture used in this study consisted of four blocks, each comprising four layers (Fig. 3). The first layer of each block was a *convolutional* layer (Fig. 3A). Each convolutional layer was composed of a set of different kernels. These kernels are essentially structure detectors that search for particular geometric shapes in the input images by performing a convolution operation. Traditionally, particular kernel shapes are designed by an engineer to perform a certain task. A CNN learns which kernel shapes are the most suited to perform the task at hand.

In order to interpret the output of the convolutional layer,

Table 1
Image acquisition parameters of the patients' CT scans used in this study.

Patient ID	Scanner Type	Reconstruction Kernel	Voxel size	Slice thickness (mm)	Tube voltage (kVp)	Tube Current (mA)
1	GE Discovery CT750 HD	BONEPLUS	0.47	0.625	120	200
2	GE Discovery CT750 HD	BONEPLUS	0.543	0.625	120	200
3	GE Discovery CT750 HD	BONEPLUS	0.49	1.25	140	626
4	GE Discovery CT750 HD	BONEPLUS	0.553	0.625	120	200
5	GE Discovery CT750 HD	BONEPLUS	0.504	0.625	120	200
6	Siemens Sensation 64	H31s	0.482	1	120	213
7	Siemens Sensation 64	H70h	0.568	0.75	120	300
8	Siemens Sensation 64	H70h	0.459	0.75	120	300
9	Siemens Sensation 64	H32s	0.4	0.6	120	380
10	Siemens Sensation 64	H60s	0.443	1	120	323
11	Siemens Somatom Definition AS+	J30s/3	0.404	1.5	120	80
12	Siemens Somatom Definition AS+	J70h/1	0.391	1	120	131
13	Siemens Somatom Definition AS+	J30s/3	0.412	1	120	113
14	Siemens Somatom Definition AS+	J70h/1	0.342	1	120	115
15	Siemens Somatom Force	Hr64h\1	0.432	1	120	184
16	Siemens Somatom Force	Hf38s/3	0.45	1	120	164
17	Siemens Somatom Force	Hr64h\1	0.39	1	120	166
18	Philips iCT 256	UB	0.513	0.9	120	131
19	Philips iCT 256	D	0.52	0.9	120	131
20	Philips Brilliance 64	UC	0.486	1	120	149

CT slice (512x512)

Patch (33x33)

Fig. 2. Patch acquisition from CT slices. Box A illustrates the confined rectangular region of interest enclosing all bone voxels in the CT slice, and box B represents the selected patch.

additional layers were included in the CNN architecture. An *activation* layer (Fig. 3B), i.e., rectified linear units (ReLU), was applied immediately after each convolutional layer to introduce a non-linear property to the CNN. This subsequently increased the flexibility of the CNN to detect different anatomical structures [9]. The output of the activation layer was normalized for numerical stability using a *normalization* layer (Fig. 3C) [45]. The last layer in each block was the *pooling* layer (Fig. 3D), which achieved spatial invariance in the detected structures [46].

After the four blocks, a final *classification* layer was used in the CNN architecture. This layer quantified the difference between the CNN prediction and the gold standard labels in each iteration of the training procedure. After each iteration, the kernels were refined in order to reduce the difference in the next iteration. Generally, a CNN is initiated with random kernel structures that are refined during training until the performance of the CNN no longer improves. In other words, the training of CNNs is characterized by identifying which kernel structures are relevant to solve the task at hand.

3.5. Implementation details

The sizes of the convolution kernels were set to 7x7 for the first layer, 5x5 for the second and third layers, and 3x3 for the final layer. Max-pooling operations were performed in the pooling layers using 2x2 kernels. Moreover, dropout [47] was applied after each convolutional layer with a value of 0.1. Training was performed using a batch size of 128 patches. In addition, the RMSprop optimizer [48] was used to update the kernel weights. In this context, the learning rate (α) and the decay (d) were set to $\alpha = 0.005$ and $d = 0.01$.
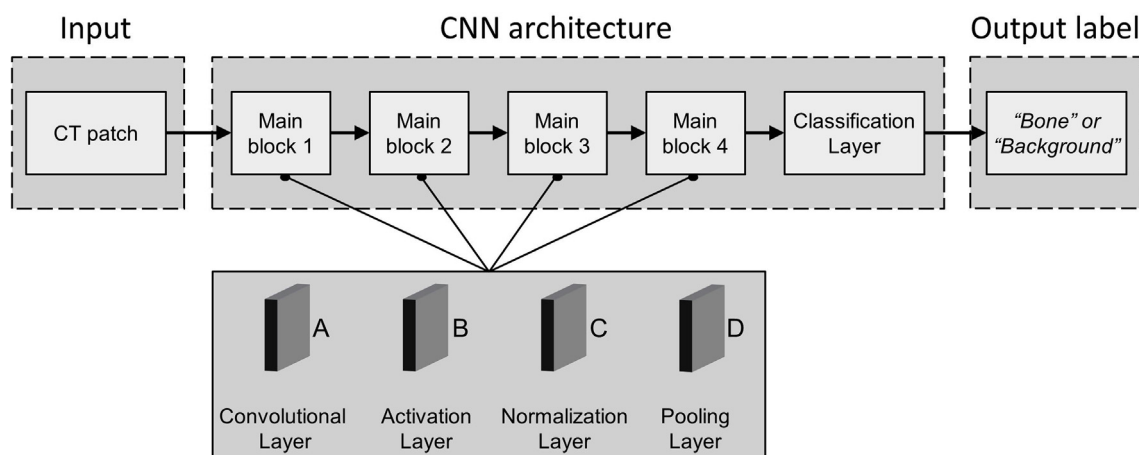
Fig. 3. Schematic overview of the CNN architecture.

CNN training (Fig. 1, step 'E') was performed using a Linux desktop computer (HP Workstation Z840) with 64 GB RAM, a Xeon E5-2687 v4 3.0GHZ CPU, and a GTX 1080 Ti GPU card. Implementation of the code was performed in Keras [49], a python library that compiles symbolical expressions into C/CUDA code that can then run on GPUs. The training of the CNN took approximately 5 min for each epoch, while the segmentation of one CT slice took approximately 20 s.

3.6. CNN performance testing

The performance of the CNN was evaluated by segmenting CT scans that were not used for training purposes (Fig. 1, step 'F'). To this end, the CNN was trained using a leave-2-out scheme: patches were acquired alternately from 18 of the 20 CT scans, after which the CNN was used to segment the 2 CT scans that were not used for training. Segmentations of the CT scans were performed by classifying each voxel individually. For this purpose, patches (33x33) were generated around each voxel in the CT scan. These patches were subsequently forwarded through the trained CNN, which resulted in label predictions (i.e., "bone" or "background") of all voxels.

The quality of the CNN segmentation was evaluated using the Dice similarity coefficient (DSC). The definition of the DSC is given in Equation (2), where TP is the number of true positives, FP is the number of false positives, and FN is the number of false negatives.

$$DSC = \frac{2TP}{2TP + FP + FN} \tag{2}$$

The TP, FP, and FN of the CNN segmentations were calculated with respect to the gold standard labels. Since these gold standard labels were derived from STL models that were often cropped to a specific region of interest and thus did not always cover all bony structures in the original CT scan, the TP, FP, and FN values were only calculated within this region of interest.

All 20 CT scans segmented using the CNN were subsequently converted into STL models using 3D Slicer software (Fig. 1, step 'G'). The resulting STL models were geometrically compared with the corresponding gold standard STL models using the surface comparison function in GOM Inspect® software. This surface comparison was performed on the largest connected component of the STL models and computes the perpendicular distance between each polygon point on the gold standard STL model and the corresponding CNN-based STL model. Signed deviations between −5.0 mm and +5.0 mm were measured between the CNN-based STL models and the gold standard STL models (Fig. 1, step 'H'). The mean deviations and standard deviations (SDs) were calculated for all CNN-based STL models of the skulls as well as for a manually selected region around the edges of each skull defect.

4. Results

Fig. 4 shows axial CT slices of four patients with a skull defect as well as the corresponding gold standard labels created by a medical engineer ("gold standard segmentation"). The labels acquired using the trained CNN ("CNN segmentation") are presented in Fig. 4C. Differences between the gold standard segmentation and the CNN segmentation are visualized in Fig. 4D: correctly labeled voxels are marked in gray, false negatives in white, and false positives in black. In addition, the DSCs between the gold standard segmentations and the CNN segmentations are presented in Table 2. DSCs ranged between 0.86 (patient 7) and 0.97 (patient 12), with a mean DSC of 0.92 ± 0.04.

Fig. 5 shows four typical examples of skull STL models acquired using the trained CNN. The STL models depicted in Fig. 5 A, C, E, and G correspond to patient 7, 9, 15, and 18, respectively. The (signed) geometric deviations between these CNN-based STL models and the gold standard STL models are presented using color maps. All CNN-based STL models generally resembled the gold standard STL models created

by the medical engineer, with mean deviations ranging between −0.19 mm ± 0.86 mm (patient 1) and 1.22 mm ± 1.75 mm (patient 7) (Fig. 6). The mean of the absolute mean deviations of all CNN-based STL models was 0.44 mm ± 0.36 mm. No differences were observed between the mean deviations of the STL models acquired using the six different CT scanners included in this study, namely, GE Discovery CT750 HD, Siemens Sensation 64, Siemens Somatom Definition AS+, Siemens Somatom Force, Philips iCT 256, and Philips Brilliance 64 (Fig. 6).

Furthermore, the edges of the skull defects in the CNN-based STL models were typically well represented with smooth boundaries. In 17 of the CNN-based STL models, the edges of the skull defects demonstrated smaller mean deviations than the whole skull (Fig. 7). The mean of the absolute mean deviations of all defect edges was 0.27 mm ± 0.29 mm.

5. Discussion

The CT-to-STL conversion currently required in medical AM remains a challenge. This is impeding the wide-spread use of additive manufactured constructs in clinical settings. Therefore, the present study aimed to develop and train a CNN for automated CT image segmentation of bone.

The bone segmentation performance of the trained CNN was good (Fig. 4). Differences between the gold standard segmentation and the CNN segmentation were generally in the order of magnitude of one voxel, which is illustrated in Fig. 4D. More specifically, the DSCs varied between the different CT scans with a mean DSC of 0.92 ± 0.04 (Table 2). These results are in good agreement with those reported by Powell et al. [34] (2017), who used a fully-automated atlas-based approach for the segmentation of temporal bones and obtained DSCs ranging between 0.58 and 0.91. Moreover, the mean DSC found in the present study is comparable to the results reported by Fu et al. [50] (2017) who proposed an atlas-based method and achieved a mean DSC of 0.94 ± 0.01 when segmenting the mandible. Torosdagli et al. [51] (2017) developed a 3D gradient-based fuzzy connectedness method for the segmentation of the mandible and reported a DSC of 0.91. Furthermore, the DSCs found in the present study are higher than those reported by Jafarian et al. [14] (2014) and Ghadimi et al. [52] (2016), who segmented cranial bones of neonates using a level-set method and achieved mean DSCs of 0.87 and 0.81, respectively. It must be noted, however, that the differences between the DSCs across studies must be interpreted with caution due to the variances in the datasets used.

All CNN-based STL models generally resembled the gold standard STL models initially created by an experienced medical engineer (Fig. 5). Interestingly, the skull CNN-based STL models resulted in an absolute mean deviation of 0.44 mm ± 0.36 mm (Fig. 6), whereas the selected region around the defect edges of the skull resulted in a smaller absolute mean deviation of 0.27 mm ± 0.29 mm (Fig. 7). These differences could have been caused by the medical engineer manually removing all noise residuals and smoothening the defect edges of the gold standard STL models to ensure the skull implant had a good fit. Since these gold standard STL models were used to generate training data, the CNN learned to reproduce these smooth and accurate defect edges in its segmentation.

Another finding in the present study was that 18 of the 20 CNN-based STL models were larger than the gold standard STL models (Fig. 6). This phenomenon could be the result of the balanced dataset that was used for CNN training containing a higher proportion of bone voxels than the original CT scans. This implies that the CNN learned to label more voxels as bone when compared with the gold standard (Fig. 4). However, there is currently no general consensus in the literature on the effect of the distribution of the training data, namely balanced or unbalanced, on the performance of CNNs [53–55]. The optimal data distribution most likely depends on the specific properties and features of the dataset. Further work is therefore required to
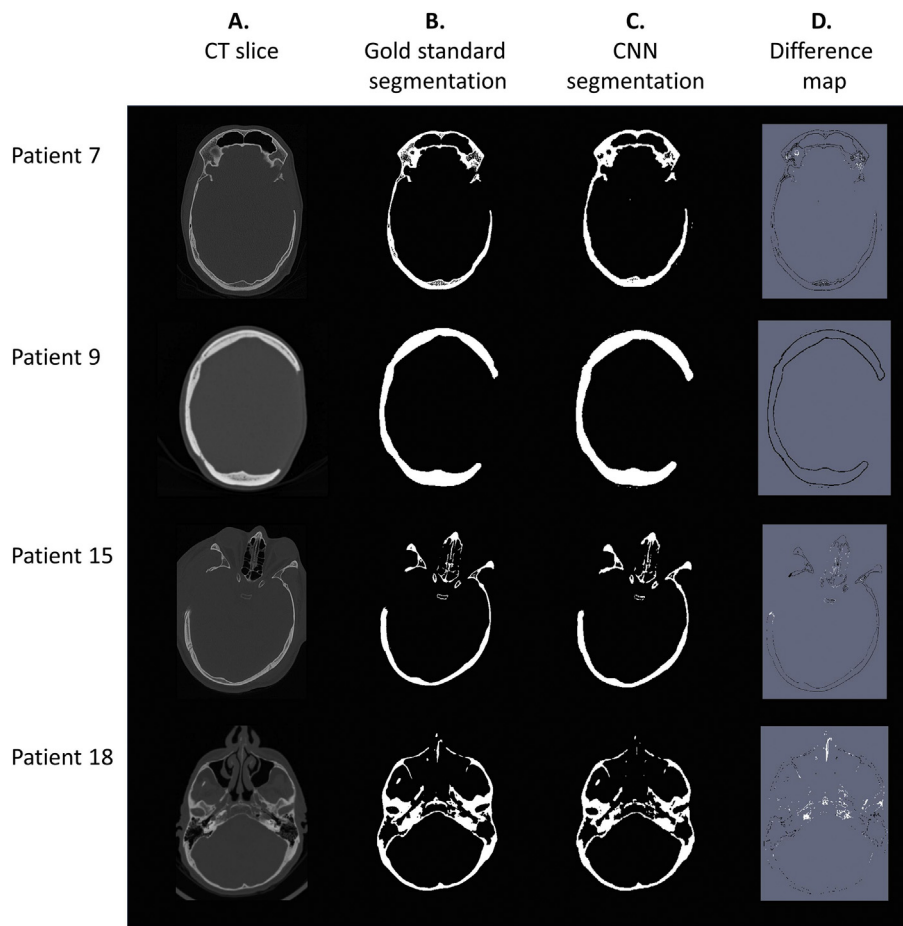
Fig. 4. Example of four axial CT slices of patients with a skull defect (A), the corresponding gold standard segmentation (B), the CNN segmentation (C), and the differences between the gold standard segmentation and the CNN segmentation (D).

Table 2
Dice similarity coefficient (DSC) between the gold standard segmentation and the CNN segmentation of all patient CT scans.

Patient ID	DSC
1	0.96
2	0.93
3	0.89
4	0.95
5	0.89
6	0.93
7	0.86
8	0.91
9	0.87
10	0.94
11	0.88
12	0.97
13	0.90
14	0.96
15	0.92
16	0.93
17	0.95
18	0.96
19	0.97
20	0.92
Mean	**0.92 ± 0.04**

The mean deviations of the CNN-based STL models in this study ranged between $-0.19\,mm \pm 0.86\,mm$ and $1.22\,mm \pm 0.39\,mm$ (Fig. 6). These results differ from those reported by Rueda et al. [56] (2006), who calculated a mean geometrical distance of $1.63\,mm \pm 1.63\,mm$ using a fully-automated active appearance model for the segmentation of cortical bone in the skull. However, the mean deviations found in the present study are comparable with those acquired using a fully-automatic atlas-based segmentation method developed by Steger et al. [20] (2012) that resulted in a mean deviation of 0.84 mm. The aforementioned findings suggest that CNNs offer comparable bone segmentation performance to the fully-automated segmentation methods currently used in medical AM.

Another interesting finding was that the six different CT scanners used in this study did not seem to have an effect on the mean deviations of the CNN-based STL models (Figs. 6 and 7). This indicates that the CNN was able to generalise intensity variations between different CT scanners and imaging protocols. In comparison, traditional rule-based segmentation methods, such as global thresholding, typically do not generalise well because they are based on a fixed set of features in images, e.g., intensities. A major advantage of CNNs is that they can automatically learn which characteristic features are relevant to segment bone in multiple CT scans, which allows the CNN to segment bone in new, unseen CT scans.

Recent advances in CNN architectures for segmentation have led to the development of fully convolutional neural networks (fCNNs) [27,57,58]. fCNNs take input images of varying sizes and produce a probability map, rather than a classification output for a single voxel. This allows fCNNs to be trained more efficiently compared with CNN architectures for the classification of single voxels [57]. However, the
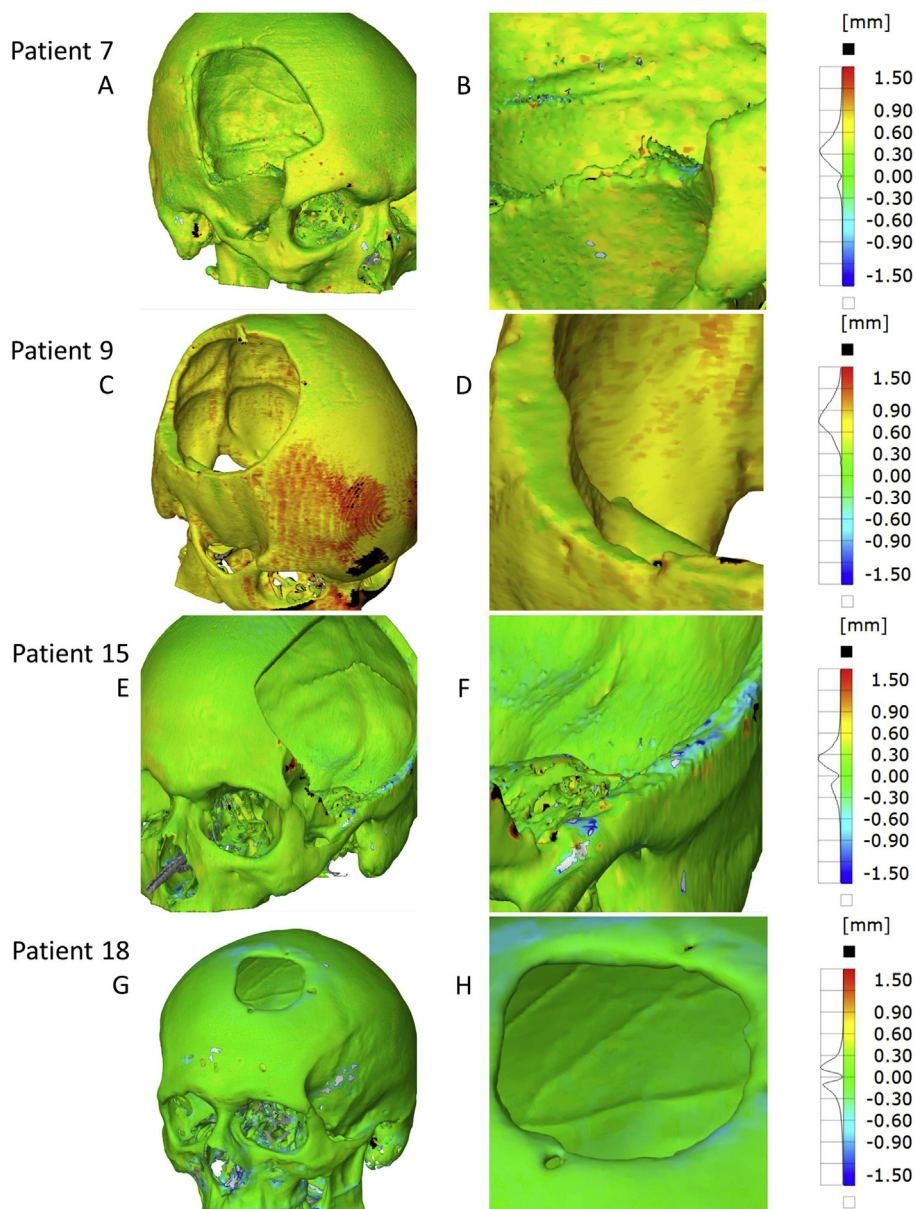
establish the viability of considering the data distribution as a tunable hyperparameter that can be optimized for specific datasets. However, this would require many (cross-validated) training sessions and would thus be a time-consuming and computationally expensive procedure.

Fig. 5. Color maps of the signed geometric deviations between four typical CNN-based STL models and their corresponding gold standard STL models (A, C, E, and G). Images B, D, F, and H present a more detailed visualization of the skull defect edges.
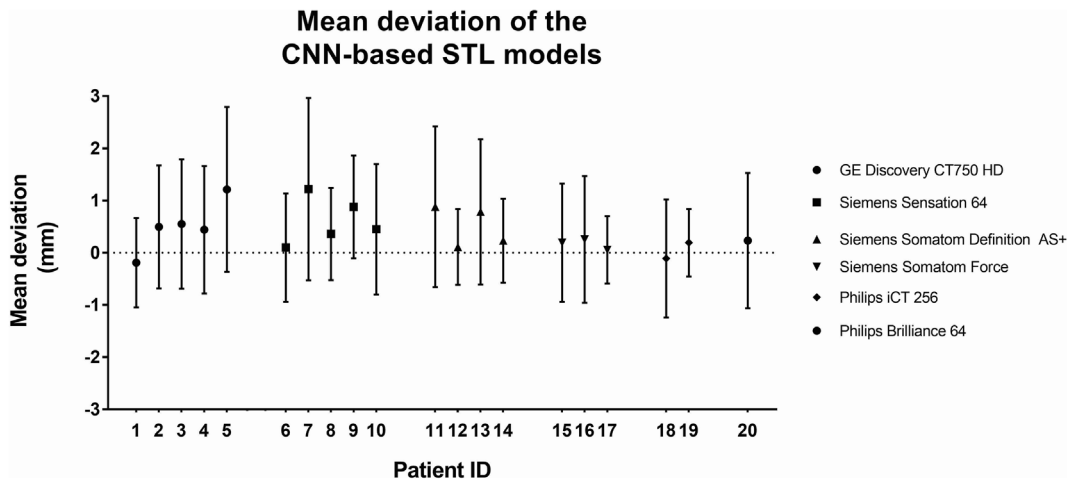

Fig. 6. Mean deviation and standard deviation (SD) of all CNN-based STL models with respect to the corresponding gold standard STL models.
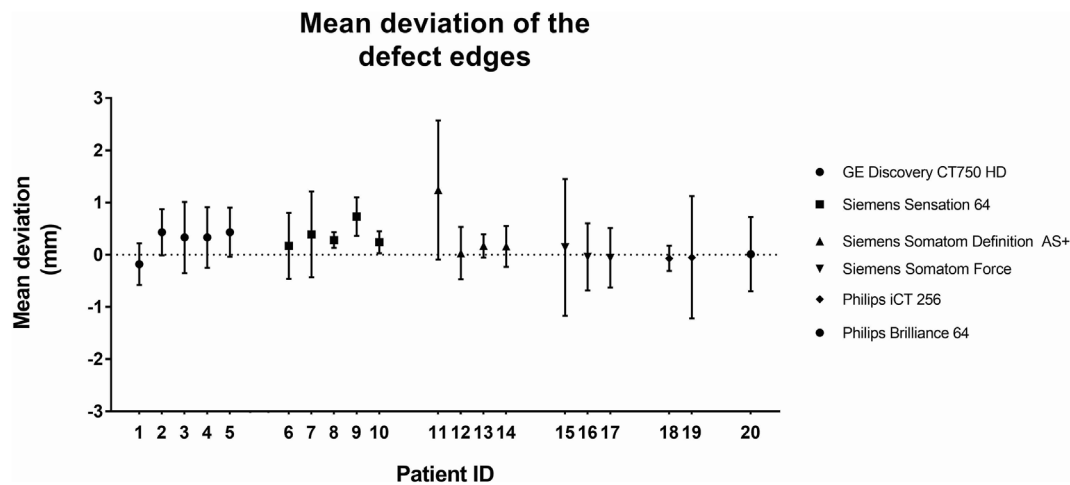
Mean deviation of the defect edges

Fig. 7. Mean deviation and standard deviation (SD) of the defect edges of all CNN-based STL models with respect to the corresponding gold standard STL models.

major challenge with fCNNs is that they require large numbers of training images [59,60]. In medical settings, the amount of data that can be acquired is often limited due to privacy regulations and ethical considerations. As a consequence, data augmentation is often necessary [60]. Therefore, the authors of the present study implemented a patch-based CNN for classification of single voxels as initially proposed by Cireşan et al. [61] (2012). This approach has been shown to perform well on multiple image segmentation tasks [62–64]. By extracting a large number of patches from multiple CT slices, sufficient input data can be acquired to train a CNN. Although patch-based CNNs are computationally less efficient than fCNNs, they are easier to train and are more robust to variations within CT slices [65].

A unique feature of the present study is that the gold standard labels that were used to train the CNN were obtained from the STL models of patients who had undergone cranioplasty using AM skull implants created by a medical engineer. Since all gold standard STL models had been successfully used to design patient-specific skull implants, their accuracy can be considered sufficient for medical purposes. One limitation of using STL models as a gold standard is the mesh-to-label conversion algorithm that is required to convert the STL models into gold standard labels. The mesh-to-label conversion algorithm implemented in 3D Slicer resulted in a small number of bone voxels incorrectly labeled as background. However, since this phenomenon was only observed in thin bony structures (≤ 1 voxel) that were not situated in the region of interest (the skull defect), it can be assumed that it did not affect the segmentation performance of the CNN.

This study presents a framework for fully-automatic CT image segmentation of bone using a CNN. The trained CNN was able to accurately segment the skull in a large variety of CT scans of patients with a skull defect. A CNN could thus help to overcome the limitations of the current image segmentation methods commonly used in medical AM, i.e., global thresholding combined with extensive and time-consuming manual post-processing. The current implementation of the CNN takes approximately 20 s to segment a CT slice, which implies that segmenting a full CT scan would take approximately an hour. Nevertheless, since the segmentation process is fully automated, the medical engineer can spend this time on other relevant tasks needed to manufacture patient-specific skull implants. Automating the image segmentation step would therefore not only reduce the subjectivity and the variance amongst medical engineers, it would also improve the cost-effectiveness of patient-specific AM constructs.

Future research should focus on the validation of the CNN using patches from multiple orthogonal planes (i.e., axial, sagittal, and coronal). Furthermore, since low-dose CT and cone-beam CT scans can be affected by higher noise levels than conventional CT scans, future studies should be undertaken to assess the performance of the CNN on low-

dose CT and cone-beam CT scans. Moreover, we suggest CNNs are trained and tested for the segmentation of other (bony) structures, such as the mandible [66] and vertebrae [39]. In addition, the segmentation performance could be further enhanced by exploring alternative CNN architectures, such as the TwoPathCNN [30] and the mixed-scale dense CNN [67], which can incorporate global features in CT scans as well as local details. Finally, new platforms and infrastructures (e.g., cloud computing) are required that allow sharing data, reproducing results, and benchmarking algorithms. This will help researchers to adapt to the rapid developments in the field of deep learning.

6. Conclusion

This study presents a CNN developed for bone segmentation that was trained using labeled CT scans of patients that had been treated using patient-specific additive manufactured skull implants. The CNN segmentation demonstrated a high overlap with the gold standard segmentation (DSC = 0.92 $\pm$ 0.04). The quality of the resulting CNN-based STL models was good (mean deviation = 0.44 mm $\pm$ 0.36 mm), particularly around the defect edges (mean deviation = 0.27 mm $\pm$ 0.29 mm). CNNs offer the opportunity of removing the prohibitive barriers of time and effort during CT image segmentation, making patient-specific AM constructs more affordable, and thus more accesible to clinicians. Further research should be undertaken to investigate the bone segmentation performance of different CNN architectures.

Conflicts of interest

None declared.

Acknowledgements

References

[1] G. Tapia, A. Elwany, A review on process monitoring and control in metal-based additive manufacturing, J. Manuf. Sci. Eng. 136 (2014) 060801, https://doi.org/10.1115/1.4028540.

[2] B.C. Gross, J.L. Erkal, S.Y. Lockwood, C. Chen, D.M. Spence, An evaluation of 3D printing and its potential impact on biotechnology and the chemical sciences, Anal.

Chem. (2014), https://doi.org/10.1021/ac403397r.

[3] C.L. Ventola, Medical applications for 3D printing: current and projected uses, P T: Peer-Reviewed J. Formul. Manag. 39 (2014) 704–711, https://doi.org/10.1016/j.infsof.2008.09.005.

[4] M. Salmi, K.S. Paloheimo, J. Tuomi, J. Wolff, A. Mäkitie, Accuracy of medical models made by additive manufacturing (rapid manufacturing), J. Cranio-Maxillofacial Surg. 41 (2013) 603–609, https://doi.org/10.1016/j.jcms.2012.11.041.

[5] E. Huotilainen, R. Jaanimets, J. Valášek, P. Marcián, M. Salmi, J. Tuomi, A. Mäkitie, J. Wolff, Inaccuracies in additive manufactured medical skull models caused by the DICOM to STL conversion process, J. Cranio-Maxillofacial Surg. 42 (2014), https://doi.org/10.1016/j.jcms.2013.10.001.

[6] M. van Eijnatten, R. van Dijk, J. Dobbe, G. Streekstra, J. Koivisto, J. Wolff, CT image segmentation methods for bone used in medical additive manufacturing, Med. Eng. Phys. 51 (2018) 6–16, https://doi.org/10.1016/j.medengphy.2017.10.008.

[7] M. van Eijnatten, J. Koivisto, K. Karhu, T. Forouzanfar, J. Wolff, The impact of manual threshold selection in medical additive manufacturing, Int. J. Comput. Assist. Radiol. Surg. 12 (2016) 607–615, https://doi.org/10.1007/s11548-016-1490-4.

[8] N. Sharma, L.M. Aggarwal, Automated medical image segmentation techniques, J. Med. Phys./Assoc. Med. Physicists India 35 (2010) 3–14, https://doi.org/10.4103/0971-6203.58777.

[9] A. Krizhevsky, I. Sutskever, H. Geoffrey E, ImageNet classification with deep convolutional neural networks, Adv. Neural Inf. Process. Syst. 25 (NIPS2012) (2012) 1–9.

[10] J. Kaur, S. Agrawal, R. Vig, A comparative analysis of thresholding and edge detection segmentation techniques, Int. J. Comput. Appl. 39 (2012) 29–34, https://doi.org/10.5120/4898-7432.

[11] J. Fripp, S. Crozier, S.K. Warfield, S. Ourselin, Automatic segmentation of articular cartilage in magnetic resonance images of the knee, in: N. Ayache, S. Ourselin, A. Maeder (Eds.), Medical Image Computing and Computer-assisted Intervention – MICCAI 2007, Springer Berlin Heidelberg, Berlin, Heidelberg, 2007, pp. 186–194, , https://doi.org/10.1007/978-3-540-75759-7_23.

[12] V. Grau, A.U.J. Mewes, M. Alcaniz, R. Kikinis, S.K. Warfield, Improved watershed transform for medical image segmentation using prior information, IEEE Trans. Med. Imag. 23 (2004) 447–458, https://doi.org/10.1109/TMI.2004.824224.

[13] Chunming Li, Rui Huang, Zhaohua Ding, J.C. Gatenby, D.N. Metaxas, J.C. Gore, A level set method for image segmentation in the presence of intensity inhomogeneities with application to MRI, IEEE Trans. Image Process. 20 (2011) 2007–2016, https://doi.org/10.1109/TIP.2011.2146190.

[14] N. Jafarian, K. Kazemi, H. Abrishami Moghaddam, R. Grebe, M. Fournier, M.S. Helfroush, C. Gondry-Jouet, F. Wallois, Automatic segmentation of newborns' skull and fontanel from CT data using model-based variational level set, Signal Image Video Process. 8 (2014) 377–387, https://doi.org/10.1007/s11760-012-0300-x.

[15] C. Lindner, S. Thiagarajah, J. Wilkinson, T. Consortium, G. Wallis, T. Cootes, Fully automatic segmentation of the proximal femur using random forest regression voting, IEEE Trans. Med. Imag. 32 (2013) 1462–1472, https://doi.org/10.1109/TMI.2013.2258030.

[16] N. Baka, S. Leenstra, T. van Walsum, Random forest-based bone segmentation in ultrasound, Ultrasound Med. Biol. 43 (2017) 2426–2437, https://doi.org/10.1016/j.ultrasmedbio.2017.04.022.

[17] J. Schmid, J. Kim, N. Magnenat-Thalmann, Robust statistical shape models for MRI bone segmentation in presence of small field of view, Med. Image Anal. 15 (2011) 155–168, https://doi.org/10.1016/j.media.2010.09.001.

[18] H. Lamecker, M. Seebass, H.-C. Hege, P. Deuflhard, J.M. Fitzpatrick, M. Sonka (Eds.), A 3D Statistical Shape Model of the Pelvic Bone for Segmentation, 2004, p. 1341, , https://doi.org/10.1117/12.534145.

[19] M.A. Baldwin, J.E. Langenderfer, P.J. Rullkoetter, P.J. Laz, Development of subject-specific and statistical shape models of the knee using an efficient segmentation and mesh-morphing approach, Comput. Methods Progr. Biomed. 97 (2010) 232–240, https://doi.org/10.1016/j.cmpb.2009.07.005.

[20] S. Steger, M. Kirschner, S. Wesarp, Articulated atlas for segmentation of the skeleton from head & neck CT datasets, Proceedings - International Symposium on Biomedical Imaging, 2012, pp. 1256–1259, , https://doi.org/10.1109/ISBI.2012.6235790.

[21] K.A. Powell, T. Liang, B. Hittle, D. Stredney, T. Kerwin, G.J. Wiet, Atlas-based segmentation of temporal bone anatomy, Int. J. Comput. Assist. Radiol. Surg. 12 (2017) 1937–1944, https://doi.org/10.1007/s11548-017-1658-6.

[22] H. Greenspan, B. van Ginneken, R.M. Summers, Guest editorial deep learning in medical imaging: overview and future promise of an exciting new technique, IEEE Trans. Med. Imag. 35 (2016) 1153–1159, https://doi.org/10.1109/TMI.2016.2553401.

[23] A. Prasoon, K. Petersen, C. Igel, F. Lauze, E. Dam, M. Nielsen, Deep feature learning for knee cartilage segmentation using a triplanar convolutional neural network, Lecture Notes in Computer Science, 2013, pp. 246–253, , https://doi.org/10.1007/978-3-642-40763-5_31.

[24] W. Zhang, R. Li, H. Deng, L. Wang, W. Lin, S. Ji, D. Shen, Deep convolutional neural networks for multi-modality isointense infant brain image segmentation, Neuroimage 108 (2015) 214–224, https://doi.org/10.1016/j.neuroimage.2014.12.061.

[25] A. De Brébisson, G. Montana, Deep neural networks for anatomical brain segmentation, IEEE Computer Society Conference on Computer Vision and Pattern Recognition Workshops, 2015, pp. 20–28, , https://doi.org/10.1109/CVPRW.2015.7301312.

[26] P. Moeskops, M.A. Viergever, A.M. Mendrik, L.S. de Vries, M.J.N.L. Benders,

I. Isgum, Automatic segmentation of MR brain images with a convolutional neural network, IEEE Trans. Med. Imag. 35 (2016) 1252–1261, https://doi.org/10.1109/TMI.2016.2548501.

[27] F. Milletari, N. Navab, S.-A. Ahmadi, V-Net, Fully convolutional neural networks for volumetric medical image segmentation, ArXiv:1606.04797 [Cs] http://arxiv.org/abs/1606.04797, (2016) , Accessed date: 17 August 2018.

[28] C.M. Deniz, S. Xiang, S. Hallyburton, A. Welbeck, S. Honig, K. Cho, G. Chang, Segmentation of the Proximal Femur from MR Images Using Deep Convolutional Neural Networks, ArXiv, (2017) (Published online).

[29] F. Liu, Z. Zhou, H. Jang, A. Samsonov, Z. Gengyan, R. Kijowski, Deep convolutional neural network and 3D deformable approach for tissue segmentation in muscu-loskeletal magnetic resonance imaging, Magn. Reson. Med. (2017), https://doi.org/10.1002/mrm.26841.

[30] M. Havaei, A. Davy, D. Warde-Farley, A. Biard, A. Courville, Y. Bengio, C. Pal, P.-M. Jodoin, H. Larochelle, Brain tumor segmentation with deep neural networks, Med. Image Anal. 35 (2016) 18–31, https://doi.org/10.1016/j.media.2016.05.004.

[31] R. Vivanti, A. Ephrat, L. Joskowicz, N. Lev-Cohain, O.A. Karaaslan, J. Sosna, Automatic liver tumor segmentation in follow-up CT scans, Proc. Patch-based Methods in Medical Image Processing Workshop, 2015.

[32] C. Elamri, A New Algorithm for Fully Automatic Brain Tumor Segmentation with 3-D Convolutional Neural Networks, (2016).

[33] O. Charron, A. Lallement, D. Jarnet, V. Noblet, J.-B. Clavier, P. Meyer, Automatic detection and segmentation of brain metastases on multimodal MR images with a deep convolutional neural network, Comput. Biol. Med. 95 (2018) 43–54, https://doi.org/10.1016/j.compbiomed.2018.02.004.

[34] W. Thong, S. Kadoury, N. Piché, C.J. Pal, Convolutional networks for kidney segmentation in contrast-enhanced CT scans, Comput. Methods Biomech. Biomed. Eng.: Imag. Visual. 6 (2018) 277–282, https://doi.org/10.1080/21681163.2016.1148636.

[35] A. Farag, L. Lu, H.R. Roth, J. Liu, E. Turkbey, R.M. Summers, A bottom-up approach for pancreas segmentation using cascaded superpixels and (deep) image patch labeling, IEEE Trans. Image Process. 26 (2017) 386–399, https://doi.org/10.1109/TIP.2016.2624198.

[36] H.R. Roth, L. Lu, A. Farag, H.-C. Shin, J. Liu, E.B. Turkbey, R.M. Summers, DeepOrgan: multi-level deep convolutional networks for automated pancreas segmentation, in: N. Navab, J. Hornegger, W.M. Wells, A. Frangi (Eds.), Medical Image Computing and Computer-assisted Intervention – MICCAI 2015, Springer International Publishing, Cham, 2015, pp. 556–564, , https://doi.org/10.1007/978-3-319-24553-9_68.

[37] J. Cai, L. Lu, Y. Xie, F. Xing, L. Yang, Pancreas segmentation in MRI using graph-based decision fusion on convolutional neural networks, in: M. Descoteaux, L. Maier-Hein, A. Franz, P. Jannin, D.L. Collins, S. Duchesne (Eds.), Medical Image Computing and Computer-assisted Intervention − MICCAI 2017, Springer International Publishing, Cham, 2017, pp. 674–682, , https://doi.org/10.1007/978-3-319-66179-7_77.

[38] M. Vania, D. Mureja, D. Lee, Automatic spine segmentation using convolutional neural network via redundant generation of class labels for 3D spine modeling, ArXiv:1712.01640 [Cs] http://arxiv.org/abs/1712.01640, (2017) , Accessed date: 20 August 2018.

[39] I. Išgum, B. van Ginneken, N. Lessmann, E.D. Angelini, B.A. Landman (Eds.), Iterative Convolutional Neural Networks for Automatic Vertebra Identification and Segmentation in CT Images, SPIE, 2018, p. 7, , https://doi.org/10.1117/12.2292731.

[40] F. Budin, I. Oguz, MeshToLabelMap, github, https://github.com/NIRALUser/MeshToLabelMap, (2017).

[41] A. Fedorov, R. Beichel, J. Kalpathy-Cramer, J. Finet, J.C. Fillion-Robin, S. Pujol, C. Bauer, D. Jennings, F. Fennessy, M. Sonka, J. Buatti, S. Aylward, J.V. Miller, S. Pieper, R. Kikinis, 3D slicer as an image computing platform for the quantitative imaging network, Magn. Reson. Imag. 30 (2012) 1323–1341, https://doi.org/10.1016/j.mri.2012.05.001.

[42] 3DSlicer.org, (n.d.). www.slicer.org (Accessed 23 January 2018).

[43] N. Aldenborgh, brain_segmentation, https://github.com/naldeborgh7575/brain_segmentation, (2016).

[44] J. Minnema, W. Kouw, F. Diblen, CNN for bone segmentation, Github (2018), https://doi.org/10.5281/zenodo.1164605.

[45] S. Ioffe, C. Szegedy, Batch Normalization: Accelerating Deep Network Training by Reducing Internal Covariate Shift, Arxiv, (2015), pp. 1–11.

[46] D. Scherer, A. Müller, S. Behnke, Evaluation of pooling operations in convolutional architectures for object recognition, Lecture Notes in Computer Science, 2010, pp. 92–101, , https://doi.org/10.1007/978-3-642-15825-4_10.

[47] N. Srivastava, G. Hinton, A. Krizhevsky, I. Sutskever, R. Salakhutdinov, Dropout: a simple way to prevent neural networks from overfitting, J. Mach. Learn. Res. 15 (2014) 1929–1958, https://doi.org/10.1214/12-AOS1000.

[48] G.E. Hinton, N. Srivastava, K. Swersky, Lecture 6a- Overview of Mini-batch Gradient Descent, COURSERA: Neural Networks for Machine Learning, 2012, p. 31.

[49] F. Chollet, Keras, GitHub, https://github.com/fchollet/keras, (2015).

[50] Y. Fu, S. Liu, H.H. Li, D. Yang, Automatic and hierarchical segmentation of the human skeleton in CT images, Phys. Med. Biol. 62 (2017) 2812–2833, https://doi.org/10.1088/1361-6560/aa6055.

[51] N. Torosdagli, D.K. Liberton, P. Verma, M. Sincan, J. Lee, S. Pattanaik, U. Bagci, Robust and fully automated segmentation of mandible from CT scans, 2017 IEEE 14th International Symposium on Biomedical Imaging (ISBI 2017), IEEE, Melbourne, Australia, 2017, pp. 1209–1212, , https://doi.org/10.1109/ISBI.2017.7950734.

[52] S. Ghadimi, H. Abrishami Moghaddam, R. Grebe, F. Wallois, Skull segmentation and reconstruction from newborn CT images using coupled level sets, IEEE J.

Biomed. Health Inform. 20 (2016) 563–573, https://doi.org/10.1109/JBHI.2015.2391991.

[53] F. Provost, G.M. Weiss, Learning when Training Data Are Costly: the Effect of Class Distribution on Tree Induction, (2011), https://doi.org/10.1613/jair.1199 ArXiv:1106.4557 [Cs].

[54] Haibo He, E.A. Garcia, Learning from imbalanced data, IEEE Trans. Knowl. Data Eng. 21 (2009) 1263–1284, https://doi.org/10.1109/TKDE.2008.239.

[55] G.E.A.P.A. Batista, R.C. Prati, M.C. Monard, A study of the behavior of several methods for balancing machine learning training data, ACM SIGKDD Explorations Newsletter - Special Issue on Learning from Imbalanced Datasets, vol 6, 2004, pp. 20–29, , https://doi.org/10.1145/1007730.1007735.

[56] S. Rueda, J.A. Gil, R. Pichery, M. Alcañiz, Automatic segmentation of jaw tissues in CT using active appearance models and semi-automatic landmarking., Medical Image Computing and Computer-Assisted Intervention : MICCAI, International Conference on Medical Image Computing and Computer-assisted Intervention, vol. 9, 2006, pp. 167–174, , https://doi.org/10.1007/11866565_21.

[57] J. Long, E. Shelhamer, T. Darrell, Fully convolutional networks for semantic segmentation, ArXiv:1411.4038 [Cs] http://arxiv.org/abs/1411.4038, (2014) , Accessed date: 20 August 2018.

[58] O. Ronneberger, P. Fischer, T. Brox, U-net: convolutional networks for biomedical image segmentation, Medical Image Computing and Computer-assisted Intervention – MICCAI 2015, 2015, pp. 234–241, , https://doi.org/10.1007/978-3-319-24574-4_28.

[59] J. Bernal, K. Kushibar, M. Cabezas, S. Valverde, A. Oliver, X. Lladó, Quantitative analysis of patch-based fully convolutional neural networks for tissue segmentation on brain magnetic resonance imaging, ArXiv:1801.06457 [Cs] http://arxiv.org/abs/1801.06457, (2018) , Accessed date: 20 August 2018.

[60] B. Kayalibay, G. Jensen, P. van der Smagt, CNN-based segmentation of medical imaging data, ArXiv:1701.03056 [Cs] http://arxiv.org/abs/1701.03056, (2017) , Accessed date: 20 August 2018.

[61] D. Ciresan, A. Giusti, L.M. Gambardella, J. Schmidhuber, Deep neural networks segment neuronal membranes in electron microscopy images, in: F. Pereira, C.J.C. Burges, L. Bottou, K.Q. Weinberger (Eds.), Advances in Neural Information Processing Systems, vol 25, Curran Associates, Inc., 2012, pp. 2843–2851 http://papers.nips.cc/paper/4741-deep-neural-networks-segment-neuronal-membranes-in-electron-microscopy-images.pdf.

[62] S. Pereira, A. Pinto, V. Alves, C.A. Silva, Brain tumor segmentation using convolutional neural networks in MRI images, IEEE Trans. Med. Imag. 35 (2016) 1240–1251, https://doi.org/10.1109/TMI.2016.2538465.

[63] C. Wachinger, M. Reuter, T. Klein, DeepNAT: deep convolutional neural network for segmenting neuroanatomy, Neuroimage 170 (2018) 434–445, https://doi.org/10.1016/j.neuroimage.2017.02.035.

[64] S. Trebeschi, J.J.M. van Griethuysen, D.M.J. Lambregts, M.J. Lahaye, C. Parmar, F.C.H. Bakers, N.H.G.M. Peters, R.G.H. Beets-Tan, H.J.W.L. Aerts, Deep learning for fully-automated localization and segmentation of rectal cancer on multiparametric MR, Sci. Rep. 7 (2017), https://doi.org/10.1038/s41598-017-05728-9.

[65] L. Hou, D. Samaras, T.M. Kurc, Y. Gao, J.E. Davis, J.H. Saltz, Patch-based convolutional neural network for whole slide tissue image classification, 2016 IEEE Conference on Computer Vision and Pattern Recognition (CVPR), IEEE, Las Vegas, NV, USA, 2016, pp. 2424–2433, , https://doi.org/10.1109/CVPR.2016.266.

[66] B. Qiu, J. Guo, J. Kraeima, R. Borra, M. Witjes, P. van Ooijen, 3D Segmentation of Mandible from Multisectional CT Scans by Convolutional Neural Networks, OpenReview.Net., 2018.

[67] D.M. Pelt, J.A. Sethian, A mixed-scale dense convolutional neural network for image analysis, Proc. Natl. Acad. Sci. Unit. States Am. 115 (2018) 254–259, https://doi.org/10.1073/pnas.1715832114.